Test of a Staggered PRT Scheme for the French Radar Network

P. TABARY, L. PERIER, J. GAGNEUX, AND J. PARENT-DU-CHATELET

Centre de Météorologie Radar, Direction des Systèmes d'Observation, Météo France, Trappes, France

(Manuscript received 11 February 2004, in final form 9 September 2004)

ABSTRACT

This paper describes the test of a staggered PRT scheme for the French radar network. The design of the staggered scheme has been done in the following context: 1) the scheme is meant to be implemented on existing C-band and S-band radars of the network, the PRF of which cannot, for technical reasons, be increased above their current values (300–400 Hz for C band and 250–300 Hz for S band); 2) the minimum expected Nyquist velocity should be around 30 m s^{-1}; and 3) the Doppler information will essentially be used to retrieve a VAD wind profile and for data assimilation by operational nonhydrostatic numerical prediction models. An operational C-band radar of the network, located in Trappes, near Paris, has been modified in order to allow Doppler processing and a dual-PRT staggered scheme with two low PRFs (PRF_1=310 and PRF_2=360 Hz corresponding to a ratio of 6/7) has been implemented. Two months of data (July–August 2003) have been analyzed. The performance of the scheme is assessed qualitatively and quantitatively through the computation of the error structure of the various velocities: velocity at PRF_1, velocity at PRF_2, and combined velocity. The sensitivity of the error structure on the signal-to-noise ratio is documented. A 7 km × 7 km median filter is introduced to reduce dealiasing errors.

1. Introduction

Pulsed Doppler radars measure the radial velocity of targets within an unambiguous interval called the Nyquist interval $[-V_N, V_N]$. The Nyquist velocity V_N is directly related to pulse repetition frequency (PRF) and to the radar wavelength (λ) as follows (Doviak and Zrnic 1984):

$$V_N = \lambda.\mathrm{PRF}/4. \quad (1)$$

True radial velocities outside the Nyquist interval (i.e., higher than V_N or smaller than $-V_N$) will appear folded or aliased, that is, shifted by $\pm 2kV_N$ into the Nyquist interval. Over the years, several methods have been proposed to solve velocity ambiguities: first of all, it is obvious from Eq. (1) that the Nyquist interval can be extended by simply increasing the radar PRF. However, not to mention rising range aliasing problems, this might not be possible for technical reasons. Radial velocities can be dealiased using an external wind reference such as from a nearby radiosonde or wind profiler and an assumption of spatial and temporal continuity of the measurements (Curtis and Houze 2001). The reference wind reference may also be generated internally using a modified version of the VAD analysis (Tabary et al. 2001) that is immune to aliased velocities. Such approaches, however, suffer from the fact that errors can propagate during the dealiasing process contaminating the whole dataset. More recently, dual-PRF schemes have been studied and implemented in operational radar systems (Joe and May 2003; Holleman and Beekhuis 2003). In that case, two series of pulses at two different PRF (PRF_1 and PRF_2, $PRF_1 > PRF_2$) are alternated and allow estimating the radial velocity of targets. Then the two velocities can be combined. It can be shown (Doviak and Zrnic 1984) that the extended Nyquist interval corresponds to an equivalent PRF equal to

$$\mathrm{PRF}_{eq} = \mathrm{PRF}_1 \times \mathrm{PRF}_2/(\mathrm{PRF}_1 - \mathrm{PRF}_2). \quad (2)$$

The basic idea of the dealiasing procedure is to check all the aliases of one velocity (V_1) and choose the one leading to the smallest difference with the second one (V_2). Such schemes typically work on series of 32 or 64 pulses. Due to the rotation of the antenna—volumic radars typically scan at 15° s^{-1}—the two radial velocities, V_1 and V_2, might not be exactly representative of the same resolution volume. In conditions of high wind shear or on the edges of cluttered areas, this can lead to dealiasing errors (Joe and May 2003). So-called staggered pulse repetition time (PRT) schemes on the other hand do not have such problems as the PRT is alternated every other pulse and the two series of pulses are completely interleaved (Zrnic and Mahapatra 1985; Gray et al. 1989). Sachidananda and Zrnic (2002) have shown recently how to overcome the main drawback of staggered PRT,

Corresponding author address: P. Tabary, Centre de Météorologie Radar, Direction des Systèmes d'Observation, Météo France, 7, rue Teisserenc-de-Bort, 78195 Trappes, France. E-mail: pierre.tabary@meteo.fr

namely the impossibility to perform spectral processing of such sequences, and a staggered PRT will soon be adopted for the Weather Surveillance Radar–1988 Doppler (WSR–88D) radars (Zrnic and Zahrai 2003).

In this paper, we present the results of an evaluation of a staggered PRT scheme that has been implemented on one of the radars of the French radar network. In section 2, we present the characteristics of the radar and give a description of the staggered scheme. The performances of the scheme are qualitatively illustrated and commented on in section 3. The error structure of the different velocities (velocity V_1 at lag PRT_1, velocity V_2 at lag PRT_2 and combined velocity $V_{combined}$) is given in section 4. Results are finally summarized in section 5. This work is the first step of a plan to use Doppler radial winds operationally. It will be completed by a quantitative evaluation of the products by comparison with radiosondes, wind profiler measurements and numerical model analyses.

2. Description of the dual-PRT staggered scheme

The design of the dual-PRT staggered scheme has been done in the following context: 1) the scheme is meant to be implemented on existing C-band and S-band radars of the network, the PRF of which cannot, for technical reasons, be increased above their current values (300–400 Hz for C-band radars and 250–300 Hz for S-band radars); 2) the minimum expected Nyquist velocity should be around 30 m s^{-1}; and 3) Doppler information will essentially be used to retrieve a velocity–azimuth display (VAD) wind profile and also to produce filtered radial velocity maps for data assimilation purposes (following the approach developed by Lindskog et al. 2000). Ground-clutter filtering for the French radars is currently done quite satisfactorily using the pulse-to-pulse fluctuation of the received signal (Sugier et al. 2002) so it was not considered a key issue when designing the Doppler scheme. Likewise, tornadoes, mesocyclones and similar small-scale hazardous weather phenomena are not very common in France and a very high spatial resolution for the radial velocity maps is therefore not really needed.

The C-band Trappes radar, located near Paris, has been slightly modified in order to allow Doppler processing. The modifications include the implementation of a coaxial magnetron and an additional linear receiver in order to process both transmitted and received signals. The coaxial magnetron is a mandatory condition to perform Doppler processing. The radar pulses are triggered alternately at PRT_1 and PRT_2 by the radar processor. The linear receiver was configured so as to make the noise level as low as possible to enhance the clear-air detection capability of the radar. It has a dynamic range of 72 dB that is tuned optimally to match the radar noise level even if it means saturation of the most intense close-range ground-clutter targets. The noise of that receiver is –113 dBm, which given the radar constant, yields a sensitivity of –20 dBZ at 10 km and 0 dBZ at 100 km. The characteristics and volume coverage pattern (VCP) of the radar are given respectively in Table 1 and Fig. 1. Figure 2 shows a simplified block diagram of the radar, radar processor, and linear numerical receiver.

TABLE 1. Characteristics of the C-band Trappes radar.

Name	Trappes
Frequency	5.6 GHz
Nominal PRF	333 Hz
Wavelength	0.05334 m
Latitude	48°46′29″N
Longitude	02°00′32″E
Altitude	191 m ASL
PRF_1	310 Hz
V_{N1}	4.13 m s^{-1}
PRF_2	360 Hz
V_{N2}	4.80 m s^{-1}
PRF_{eq}	2232 Hz
V_N	29.76 m s^{-1}
Elevation angles	Every 5 min: 0.4°, 0.8°; every 15 min: 1.8°, 2.4°, 3.6°, 4.8°, 6.5°, 9°

Considering requirements 1) and 2) above, the two PRTs, PRT_1 and PRT_2, were set, respectively, to 1/360 and 1/310 s in a ratio of 6/7. The corresponding Nyquist velocities are respectively equal to 4.8 and 4.1 m s^{-1}. The two PRTs are very close to each other and very close to the initial PRT (1/333 s). Consequently, the duty cycle of the magnetron is kept nearly the same as in the single-PRT case. No detrimental effect of the staggered scheme on the modulator has been reported since its implementation in July 2003. Velocities at lag PRT_1 and PRT_2 are estimated using the pulse pair processing algorithm (Doviak and Zrnic 1984). The extended Nyquist velocity [Eq. (2)] is equal to 29.8 m s^{-1}. As explained in the introduction, V_1 is dealiased within $[-V_N, V_N]$ using V_2 as a reference. Raw complex covariance and reflectivity estimates are projected for each radar pulse and each range gate directly into a radar-centered Cartesian grid, the size and resolution of which are respectively 512 km × 512 km and 1 km × 1 km. The averaging process, necessary to reduce the noise on covariances estimates, takes place during this projection: given the slow antenna rotation speed (6° s^{-1}), the gate spacing (125 m) and the pulse repetition frequency (PRF) values (310 and 360 Hz), this leads on average to 1200 estimates for a 1 km^2 pixel located at 10 km from the radar and 10 times less (120) at 100 km; 100 km is often considered as the maximum range up to which radar data can be used quantitatively. Beyond that range, beam filtering and beam propagation fluctuations make the measurements less reliable though qualitatively still very useful. In the present study, four Cartesian 1-km^2 maps were produced in real time for each elevation angle: V_1, V_2, $V_{combined}$, and Z.

3. Qualitative assessment of the scheme

Typical plan position indicators (PPIs) of reflectivity and combined radial velocity are shown in Figs. 3a and

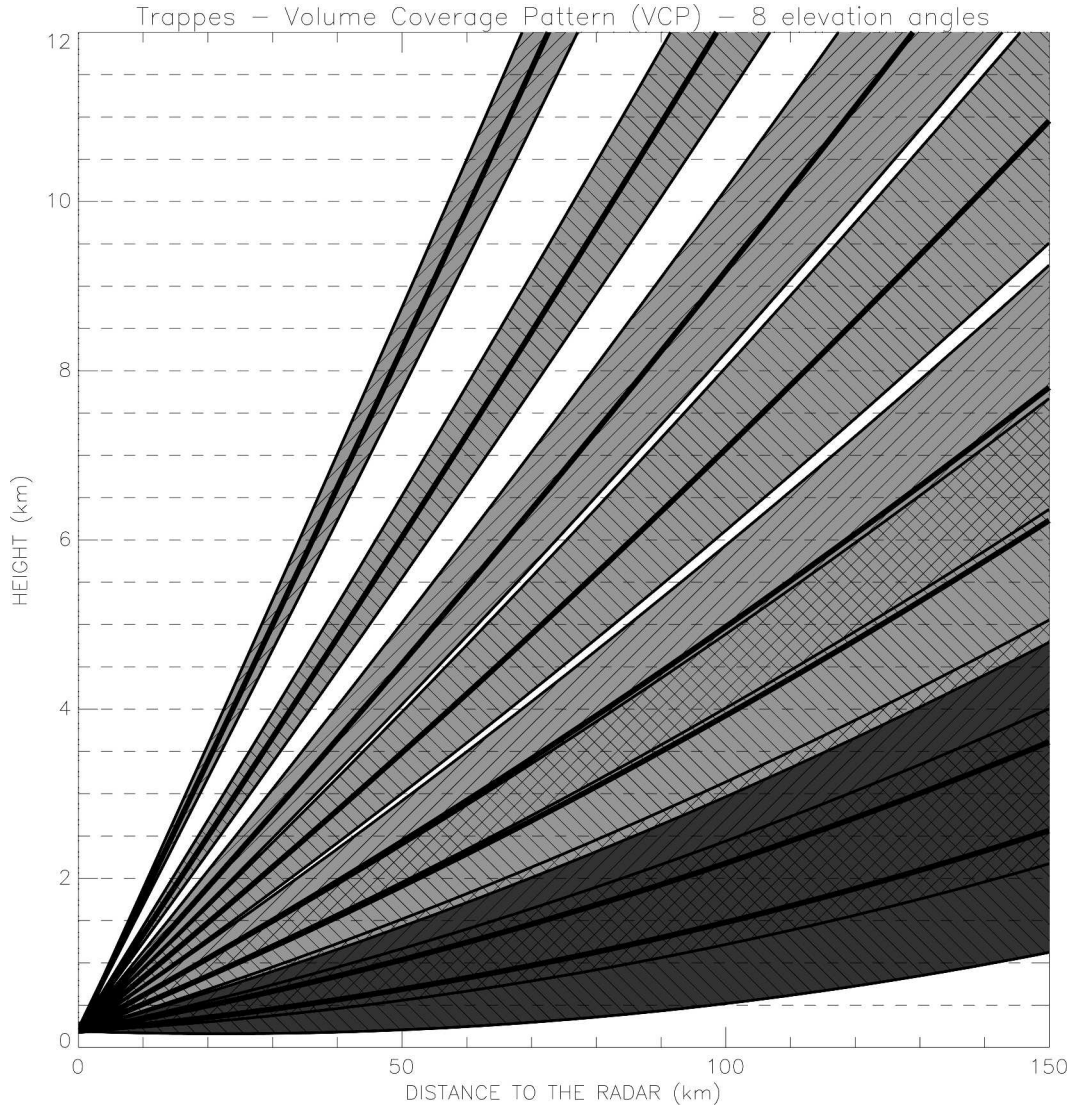

FIG. 1. Volume coverage pattern of the Trappes radar.

3b. They were obtained at an elevation angle of 0.4° at 1715 UTC on 26 July 2003. A widespread stratiform precipitating system passed over the radar on that day. As can be seen from Fig. 3b, the flow was mainly from the southwest with a maximum speed of about 26 m s^{-1}. A closer look at Fig. 3b reveals some noisy areas, most notably in the southwest and northeast corners of the domain. Dealiasing errors in those areas result in large discrepancies ($\pm 2k \times V_{N1}$; i.e., $\pm k \times 9.6$ m s^{-1}) with respect to the background field. Another way to show those dealiasing errors is by representating the combined radial velocity as a function of the azimuth for a given height. This is what is done in Fig. 4a. The sinelike shape of the curve is obvious and allows retrieving, at first-order (Browning and Wexler 1968; Waldteufel and Corbin 1979), the wind speed (about 18 m s^{-1}) and wind direction (240°). However, secondary and even higher-order traces are visible above and below the main one. They are shifted by $\pm k \times 9.6$ m s^{-1} from the main trace and are clearly identified as dealiasing failures.

To reduce the dealiasing errors, a running median filter has been introduced. The width of the window was set to 7 km × 7 km. To avoid contamination by cluttered pixels in the filtering process, only combined radial velocities above 1 m s^{-1} or below −1 m s^{-1} are used. This is a very convenient and efficient way to remove cluttered pixels even though it has the drawback of removing precipitation areas with close-to-zero radial velocities. The spectrum width would undoubtedly be a more appropriate parameter to discriminate precipitation from ground-clutter but even though it can be calculated with pulse pair processing (see Doviak and Zrnic 1984), its calculation was not in-

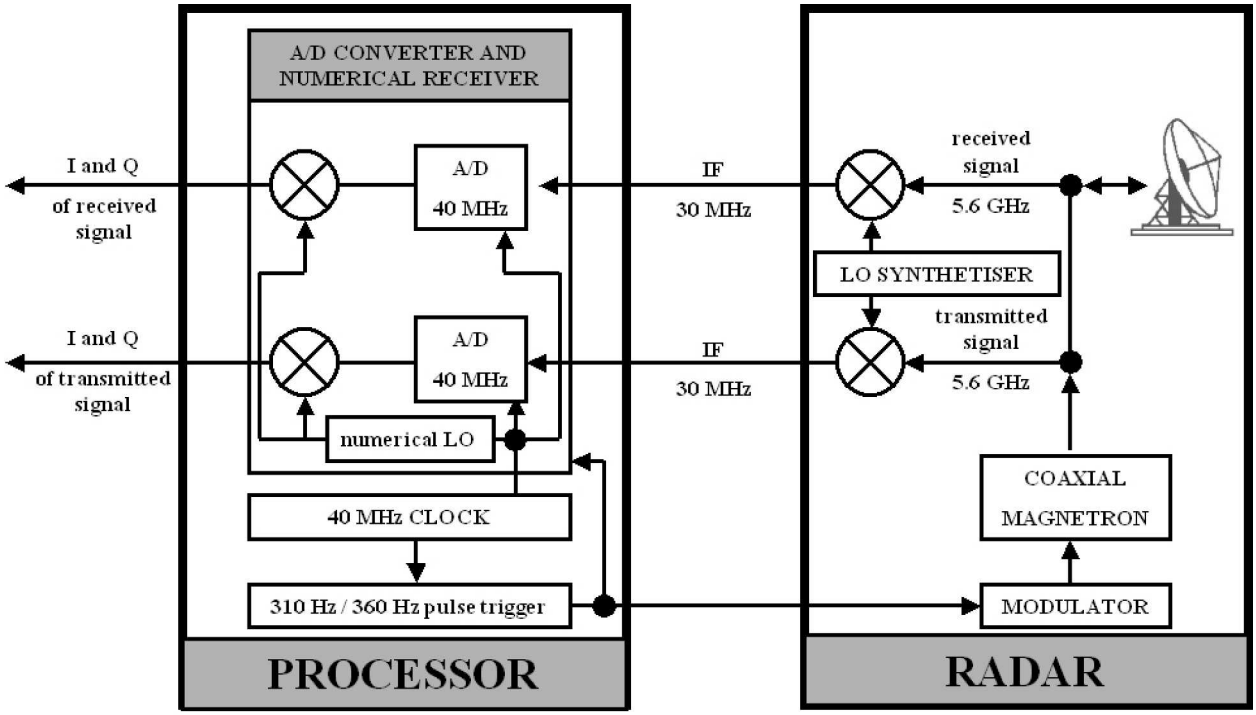

FIG. 2. Simplified block diagram of the radar, radar processor, and linear numerical receiver. Here IF stands for intermediate frequency, A/D for analog-to-digital converter, and LO for local oscillator.

cluded in the real-time processing. In the future, we plan to use the pulse-to-pulse fluctuations PPIs (Sugier et al. 2002) to identify cluttered pixels on radial velocity PPIs exactly the same way it is done for operational reflectivity PPIs. Like close-to-zero radial velocity pixels, pixels with a signal-to-noise ratio (SNR) below 3 dB are removed from the analysis. The running median filter is finally applied to the remaining pixels and the filtered value is validated only if the at least 50% of the pixels within the 7 km × 7 km filtering window are available. This filter is much simpler than the Laplacian filter introduced by Joe and May (2003). Another advantage of the median filter is that it preserves discontinuities due to aliasing within $[-V_N, V_N]$ of true radial velocities larger than (smaller than) V_N ($-V_N$). The impact of the median filter on combined radial velocities is illustrated in Figs. 3c and 4b. The noisy areas of Fig. 3a have been smoothed and the secondary traces in the velocity–azimuth representation (Fig. 4a) have disappeared. The removal of close-to-zero velocity pixels can also be seen in Figs. 3c and 4b.

Figure 5 illustrates the performances of the Doppler scheme on a difficult case (0100 UTC16 July 2003). The layout is exactly the same as for Fig. 3. The situation is much more complex with low-intensity (0–10 dBZ) clear-air echoes in the vicinity of the radar and strong convection with reflectivities as high as 50–55 dBZ in the southwest of the domain. The V_{combined} radial velocity field contains a higher fraction of dealiasing errors than in the stratiform case. This is quite consistent with the fact that the Doppler spectrum is broadened by shear and turbulence in convection, which makes the dealiasing of V_1 using V_2 less efficient. Despite the outliers, the overall structure of the radial velocity field clearly shows a maximum of about 25 m s^{-1} located between 30 and 60 km southwest of the radar. Positive radial velocities can also be seen east of the radar at about 30 km, which tends to indicate that a strong convergence is taking place over the radar just a few kilometers ahead of the convective system. The application of the 7 km × 7 km median filter is very efficient in smoothing the image while preserving the convergence pattern and the maximum radial velocity values.

Using the 7 km × 7 km median filtered radial velocities, a volume velocity processing (VVP) wind profile can be obtained assuming that the wind field is locally linear (Waldteufel and Corbin 1979). The parameters of the wind profile retrieval technique have been tuned after several tests and are largely inspired from the exhaustive study by Holleman (2003).

- Data at all elevation angles are included.
- Radial velocities up to 30 km away from the radar are taken into account.
- The u and v components of the wind are retrieved in the least squares sense assuming that the contributions of the terminal fall speed (v_T), vertical velocity (w_0), and horizontal divergence to the radial velocity

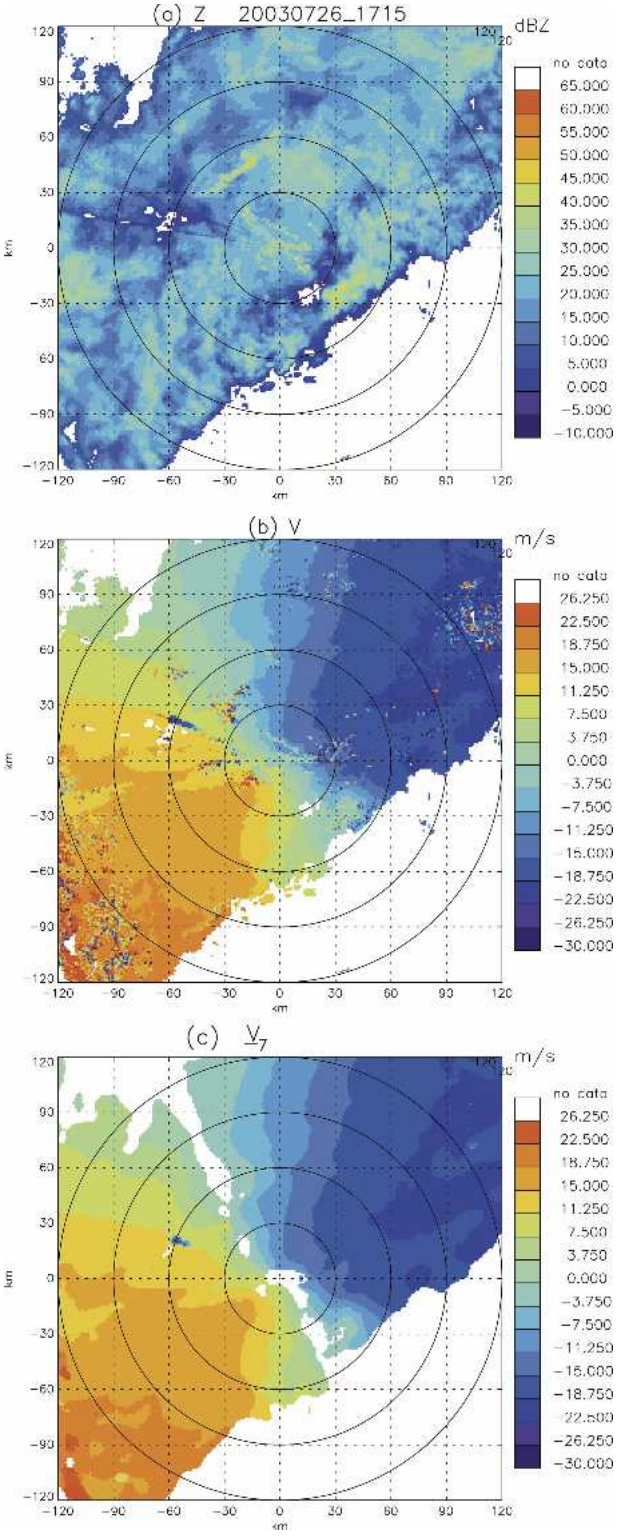

FIG. 3. (a) PPIs of reflectivity, (b) raw combined radial velocity, and (c) 7 km × 7 km median filtered combined radial velocity for the stratiform case on 1715 UTC 26 Jul 2003. The value of the elevation angle is 0.4°. North is to the top of the page.

are negligible. Notice that the highest elevation angle of the Trappes VCP is only 9°, which tends to make the contributions of v_T and w_0 very small.

- The wind is retrieved every 200 m from ground level to 10 km. However, given the VCP and the limit imposed on the maximum range (30 km), the profile cannot be retrieved above 5 km. This maximum height could be increased either by adding higher elevation angles to the VCP or by extending the maximum range (30 km) up to which radial velocities are considered. This, however, might put at risk the VAD assumption of local linearity of the wind field.
- A quality control is performed at each level on the basis of the total number of measurements taken into account in the analysis (at least 100), their azimuthal distribution (a data gap in azimuth larger than 120° is not allowed) and the statistical dispersion of measurements around the fitted sine curve (2 m s^{-1}). This last check is helpful to identify an inconsistency between the linear VAD model and the observed radial velocities that might be caused either by nonlinearities (e.g., convergence/divergence couplets) or by aliased velocities within the extended Nyquist interval [(−29.8; 29.8) m s^{-1}].

Figure 6 shows a time series of wind profiles corresponding to the 0000–1200 UTC 27 July 2003 (Fig. 6a) and 1200–2400 UTC–0000 UTC 28 July 2003 (Fig. 6b). For the sake of pedagogy, that day was preferred to the day introduced before (26 July 2003) and from which Figs. 3 and 4 are taken. It reveals indeed a mixture of clear-air detection up to 1500 m (from 0000–0600 and from 1200–2300 UTC), elevated nonprecipitating clouds (from 0000 to 0600 UTC), and rain (from 0600 to 1200 UTC). The vertical and temporal continuity of the wind barbs, though obtained with completely independent measurements, illustrate the remarkable robustness of the algorithm and the consistency of the measurements.

To evaluate more objectively the clear-air detection capability of the (C band) radar as a function of height [above sea level (ASL), the radar being at 191 m ASL], a statistical study was performed over two periods: July–August (summer), on the one hand, and September–November (fall), on the other hand. More than 4000 profiles were included in each period and Fig. 7 shows, for each level, the statistical availability of wind measurements. In the summer, wind measurements are available 90% of the time at 500 m, 80% at 1000 m, 60% at 1500 m, and 35% at 2000 m. The curve evidences a plateau at 6% above 3000 m, which corresponds to the statistical occurrence of rain in that period. The ability to retrieve nearly continuously low-level wind profiles during the summer is very promising in the perspective of data assimilation by the next-generation operational mesoscale nonhydrostatic numerical prediction models. These performances were obtained thanks to the special configuration of the lin-

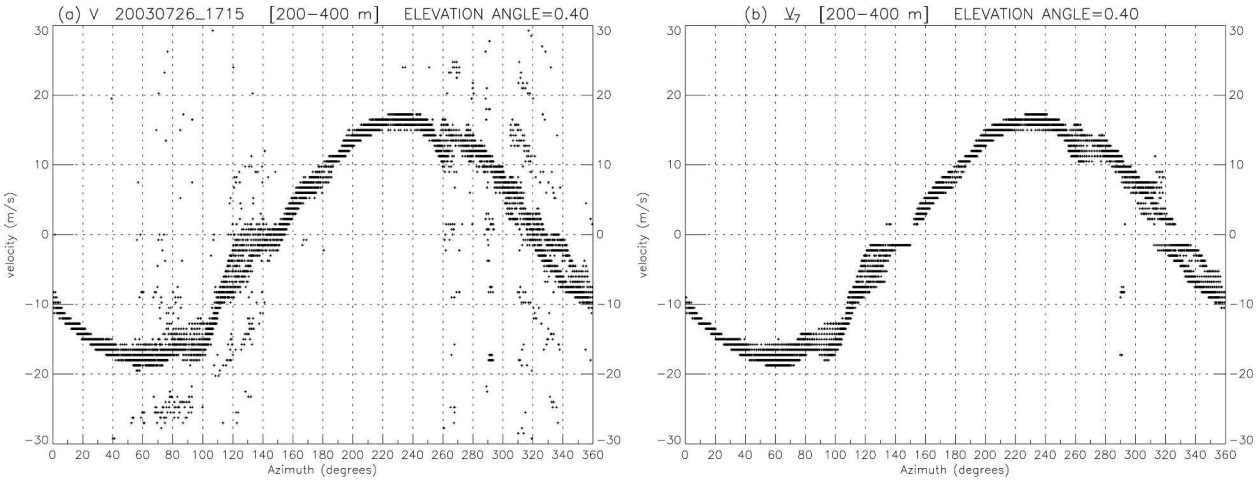

FIG. 4. (a) Representation of the raw combined radial velocity and (b) 7 km × 7 km median filtered combined radial velocity as functions of the azimuth at the height of 300 m for the 1715 UTC 26 Jul 2003. The elevation angle is 0.4°.

ear receiver. The lowest layer in which the wind profile can be retrieved is at 300 m ASL, that is to say, 100 m above ground. In the fall, wind measurements are available 75% of the time at 500 m, 55% at 1000 m, 40% at 1500 m, and 25% at 2000 m. The curve plateaus at 13% above 3000 m. The clear-air detection capability of the radar is reduced in the fall and there are less available wind measurements at low levels. Consistent with climatology, the occurrence of rain is higher in the fall than in the summer and wind measurements at higher levels (above 3000 m ASL) are more frequently available. The VAD wind profiles are currently produced in real time and monitored by the operational French ARPEGE numerical weather prediction model. If the profiles turn out to be statistically consistent with model analyses, in the sense that there is no bias and an acceptable standard deviation between the two sources of information, they will be assimilated in a second step.

4. Quantitative assessment of the scheme

It is rather difficult to evaluate quantitatively the quality of radial velocity estimates, whether at single PRT or at dual PRT or dual PRF, as no independent measurements are usually available. For instance, Gray et al. (1989) assume the radial velocity field is locally uniform, compute a mean value over a small domain and finally evaluate the standard dispersion around the mean. Assuming a Gaussian Doppler spectrum, the standard error of dual-PRT velocities can be computed analytically and its expression as a function of the SNR and the number of samples is given in appendix A of Zrnic and Mahapatra (1985). Numerical simulations can also be used to investigate the relationship between the standard error of the radial velocity and the ratio between the two PRFs (Joe and May 2003). In this section, we go a bit further and evaluate not only the standard error but also the entire error distribution as a function of the SNR. The idea of stratifying the results according to SNR values is supported by theoretical work on the expected variance of the velocity estimated by pulse pair processing (Doviak and Zrnic 1984; Gray et al. 1989). As already alluded to in the qualitative comparison of the convective and stratiform cases (Figs. 3 and 5), another relevant parameter to analyze the results would definitely be the spectrum width but unfortunately that parameter was not available. To compute the error distribution of the various radial velocities (V_1, V_2, and V_{combined}), we use the quality-checked VAD wind profiles and recreate for each elevation angle reference radial velocity maps. To be more explicit, the reference radial velocity for a given pixel is simply obtained by projecting the VAD wind vector at the appropriate level, if available, along the radar beam at the pixel location. This value of the radial velocity can then be considered as the truth against which observed velocities V_1, V_2, and V_{combined} can be compared. Possible aliasing was taken into account when comparing observed and modeled velocities, this was especially important for single-PRT velocities V_1 and V_2. The comparison was performed over the 2-month period (July–August 2003) up to 30 km away from the radar with all validated pixels of all elevation angles. We restricted the analysis to the first 30 km around the radar to make the VVP linearity assumption as valid as possible and minimize the velocity errors arising from the inadequacy of the reference. Comparaison was not done at heights where no wind measurements were available. Results are stratified according to the SNR value. Figures 8, 9, and 10 show, respectively, the statistical error distribution of V_1 and V_2 (Figs. 8a,b), V_{combined} (Fig. 9), and the statistical distribution of $V_1 - V_2$ (Fig. 10). Notice that the vertical axis is logarithmic and that the vertical scale is different

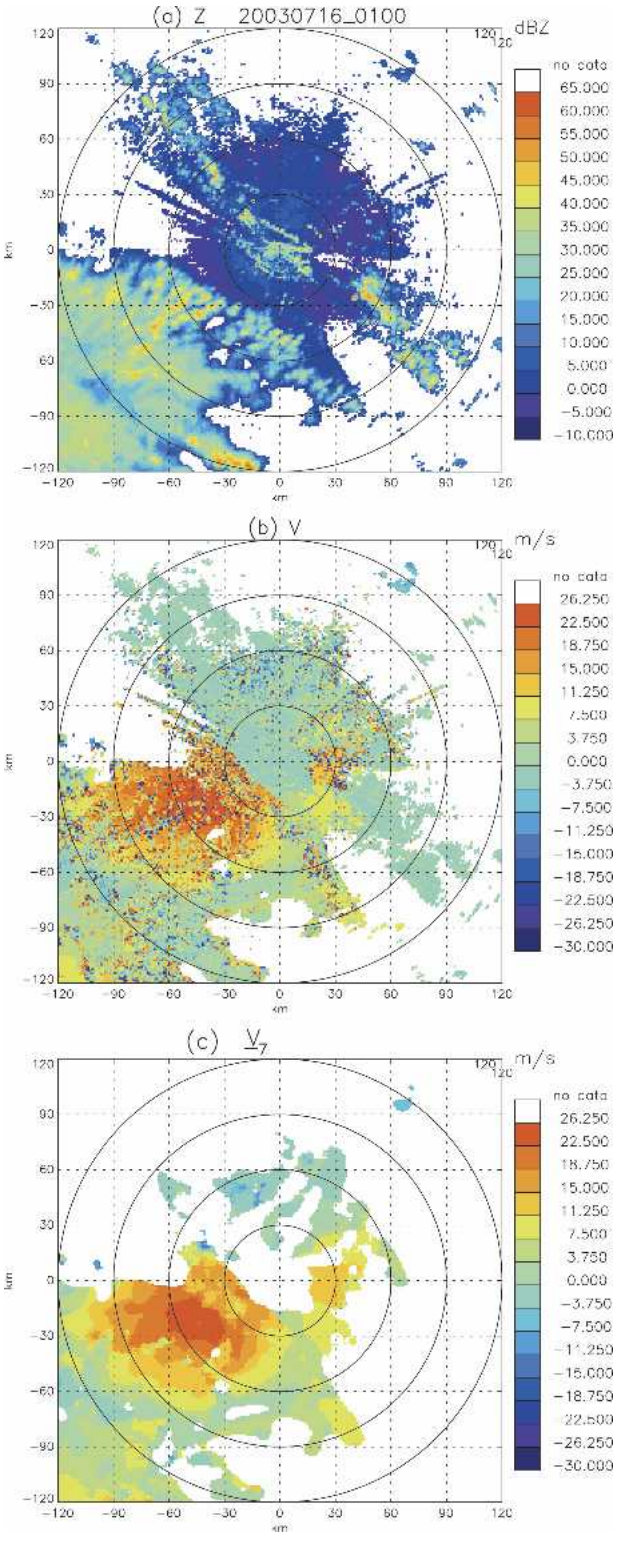

FIG. 5. (a) PPIs of reflectivity, (b) raw combined radial velocity, and (c) 7 km × 7 km median filtered combined radial velocity for the convective case on 0100 UTC 16 Jul 2003. The value of the elevation angle is 0.4°. North is to the top of the page.

between Fig. 8 and Figs. 9 and 10. All histograms have been scaled with respect to the total number of points and are expressed in percent. The error on V_1 spans $(-V_{N1}, V_{N1})$ [(−4.8, 4.8) m s^{-1}], the error on V_2 $(-V_{N2}, V_{N2})$ [(−4.1, 4.1) m s^{-1}], and the error on V_{combined} $(-V_N, V_N)$ [(−29.8, 29.8) m s^{-1}]. The distribution of V_1–V_2 spans $(-V_{N1}-V_{N2}, V_{N1} + V_{N2})$ [(−8.9, 8.9) m s^{-1}]. Before further commenting on the results, it should be emphasized at this point that all errors should be considered as upper bounds as the VAD wind profiles used for reference and might not be exactly representative of the actual wind field. Even though the analysis is restricted to the first 30 km around the radar and the VAD wind profiles have been thoroughly quality-checked, the assumption of local linearity of the wind might not be fully verified and small-scale nonlinearities (e.g., convergence/divergence couplets and strong shear) may be contributing to increase the errors.

The error distributions of V_1 and V_2 (Figs. 8a,b) are not exactly triangular, whatever the SNR may be, which indicates a small departure from Gaussianity. The error distribution of V_1 is more peaked than that of V_2, which is a clear consequence of the shorter lag time ($\text{PRT}_1 < \text{PRT}_2$) and a higher correlation. As an example, for the first class of SNR (12–15 dB), the percentage of velocities in error by ±4 m s^{-1} is equal to 1.3% for V_1 and 1.7% for V_2. At larger SNR (36–39 dB), these percentages drop down respectively to 0.6% and 0.8%, which represents a reduction by a factor of about 2. Likewise, the percentage of accurate velocities (error of 0 m s^{-1}) increases for V_1 and V_2 from 5% to 7%, respectively.

The histogram of V_{combined} (Fig. 9) has a somewhat different shape. It evidences secondary maxima shifted by $\pm 2k \times V_{N1}$ (+8.9, −8.9, +17.8, −17.8 m s^{-1}, etc.) around 0 m s^{-1} that are identified as dealiasing errors. These errors are drastically reduced when the SNR increases. As an example, the primary sidelobes (error of ±8.9 m s^{-1}) are reduced by a factor of 10 between low and high SNR values. The central part of the spectrum also becomes more peaked between low and high SNR values. The error distribution of the 7 km × 7 km median filtered velocity for all SNR values (V_7) has been superimposed on Fig. 9. As qualitatively illustrated on Figs. 3, 4, and 5, the main improvement is the reduction of the secondary maxima associated to dealiasing errors. The error distribution of V_7 appears to be slightly asymmetric but there is no physical explanation for that and this feature is probably not statistically significant. Apart from that, the central part of the error spectrum of V_7 is really close to what is obtained with the raw combined radial velocity at high SNR values.

Finally, as theoretically expected with two Nyquist velocities V_{N1} and V_{N2} in ratio of 6/7, the histogram of V_1–V_2 (Fig. 10) evidences a series of 13 peaks at 0, $\pm(-2V_{N2})$, $\pm(2V_{N1}-2V_{N2})$, $\pm(2V_{N1}-4V_{N2})$, $\pm(4V_{N1}-4V_{N2})$, $\pm(4V_{N1}-6V_{N2})$, and $\pm(6V_{N1}-6V_{N2})$. Two consecutive peaks are spaced apart by 2 (V_{N1}–V_{N2}). The

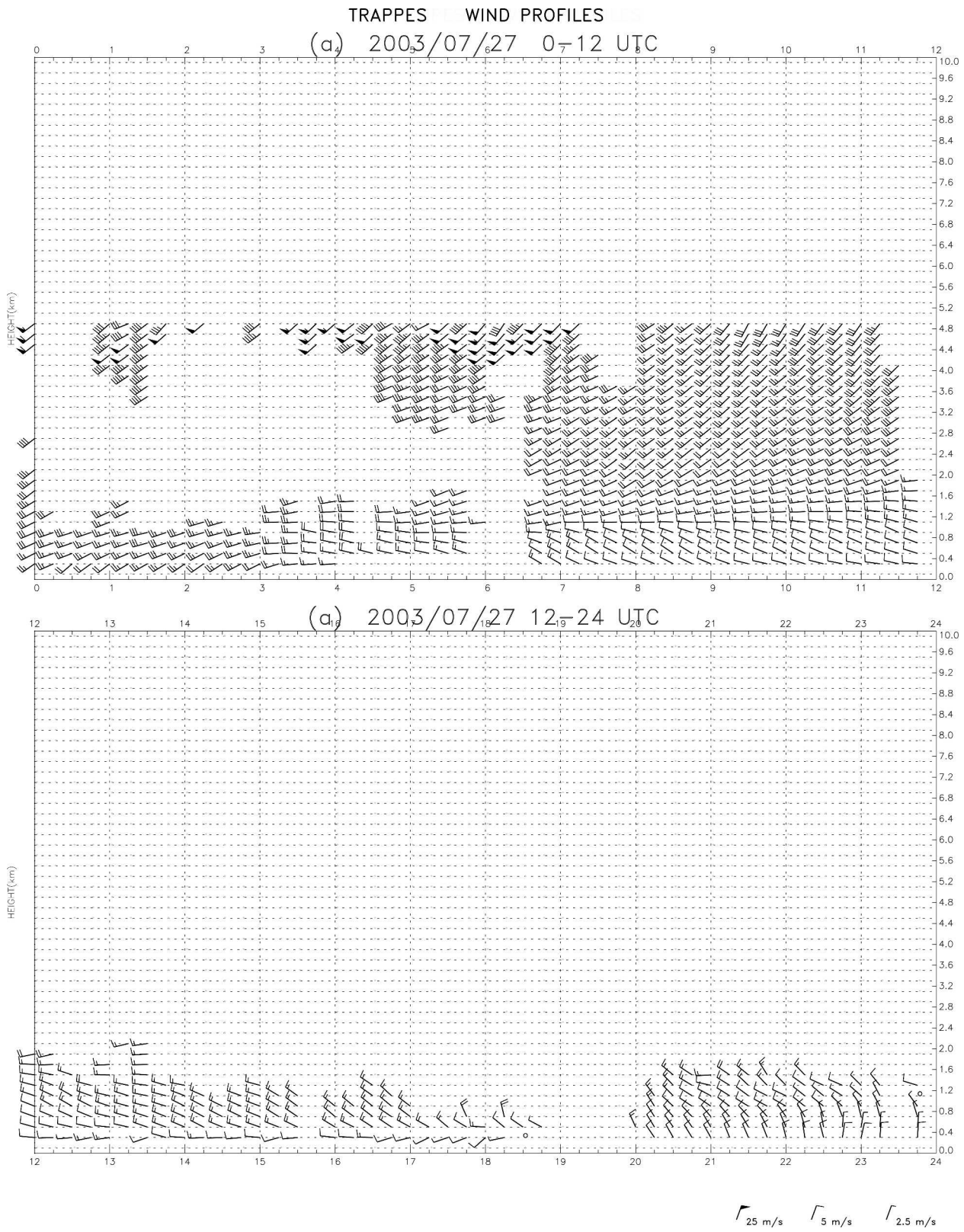

FIG. 6. Time series of the retrieved wind profiles for 27 Jul 2003.

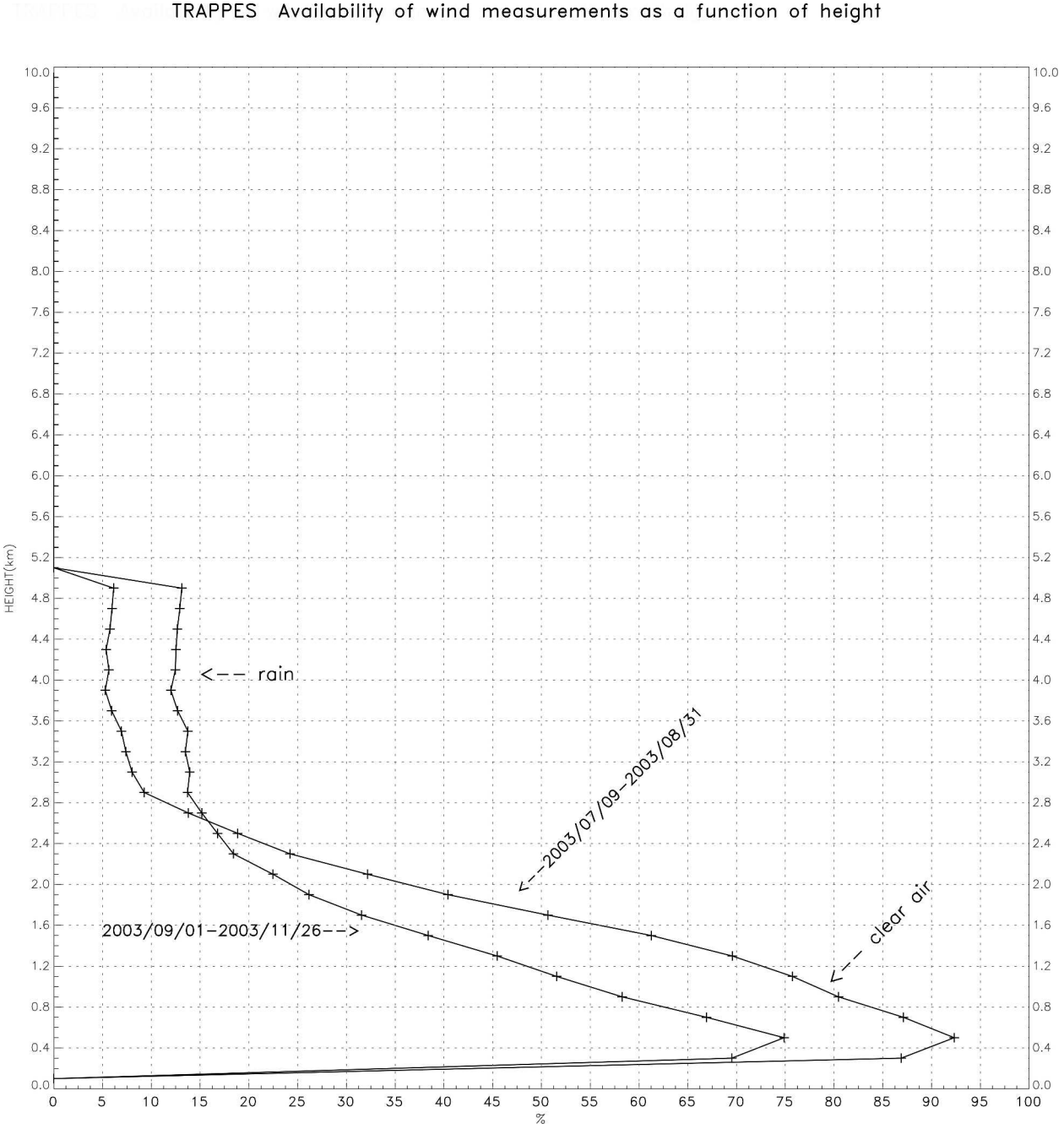

FIG. 7. Availability of wind measurements as a function of height (ASL) for Jul–Aug 2003 and Sep–Nov 2003. Recall that the Trappes radar is at the height of 191 m ASL.

relative magnitude of the different peaks depends upon the distribution of the radial velocity. In particular, the fact that the peaks around ± 4 m s^{-1} or ± 5.5 m s^{-1} are smaller than the others is simply due a smaller number of high (above 20 m s^{-1}) radial velocities in the dataset. More interestingly, it can be seen from Fig. 10 that the peaks sharpen as the SNR increases and that the shape of the spectrum tends to be more and more discrete, which would be the case in the absence of noise. Considering Fig. 10, it might be possible to implement a quality control of the combined radial velocity based on the separation between the actual value of V_1–V_2 and the theoretical possible values. This has not been investigated in the present study. Finally, given the exact values of PRT_1 and PRT_2 (1/360 and 1/310 s) and their exact ratio (31/36), the theoretical periodicity of V_1–V_2

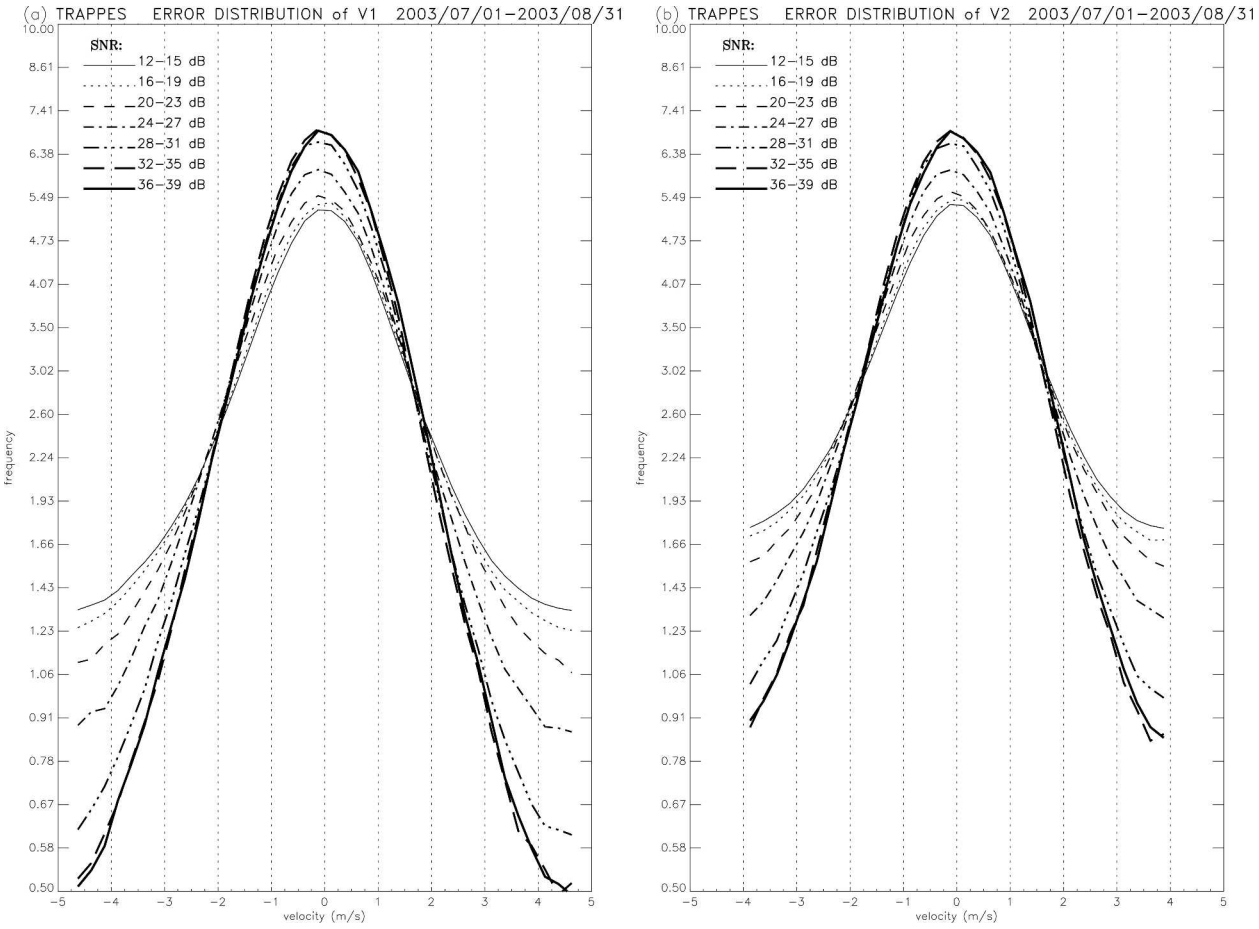

FIG. 8. Error structure of the velocities at (a) lag PRT_1 (V_1) and (b) lag PRT_2 (V_2) for different values of SNR.

is not $2V_N = 2*(31/5) \times V_{N1}$ but five times more—that is, $2 \times 31 \times V_{N1}$. The periodicity of V_1–V_2 would be exactly $2V_N$ if the ratio between PRT_1 and PRT_2 was exactly 6/7. The consequence of this tiny difference is the apparition of series of additional peaks in the V_1–V_2 distribution. However, these additional peaks are generated by radial velocities larger than (smaller than) V_N ($-V_N$). As there are very few such velocities in the data sample, this is almost not noticeable on Fig. 10 except around ± 4 m s^{-1} where a broadening of the peak can be seen.

Figure 11 shows the rms error on V_1 and V_2 as a function of the SNR, together with the rms error on the combined radial velocity with various degrees of median filtering: V_{combined} (no filtering), V_3 (median filtered over a 3 km $\times$ 3 km window), V_5 (median filtered over a 5 km $\times$ 5 km window), and V_7 (median filtered over a 7 km $\times$ 7 km window). The rms error on the raw combined radial velocity varies between 7 m s^{-1} at low SNR values and 4 m s^{-1} at higher SNR values. This is clearly unacceptable for operational purposes. The 3 km $\times$ 3 km median filter induces a significant reduction of the rms error, most notably at lower SNR values. Higher degrees of filtering (5 km $\times$ 5 km and 7 km $\times$ 7 km) contribute to further reducing the error though less and less significantly. A 7 km $\times$ 7 km median filter yields to a rms error on the radial velocity of about 2.2 m s^{-1} that is almost independent on the SNR. Recall, however, that all rms errors shown in Fig. 11 should be considered as a upper bounds as there might be local nonlinearities in the wind field even though the quality of the VAD wind profiles have been thoroughly checked and data are used only up to 30 km.

5. Summary

An operational C-band radar of the French radar network has been modified in order to allow Doppler processing. A linear receiver was added to perform Doppler processing and configured so as to make the noise level as low as possible to enhance the clear-air detection capability of the radar. A staggered PRT scheme has been implemented and tested over a 2-month period (July–August 2003). As the scheme is intended to be implemented on existing C-band and

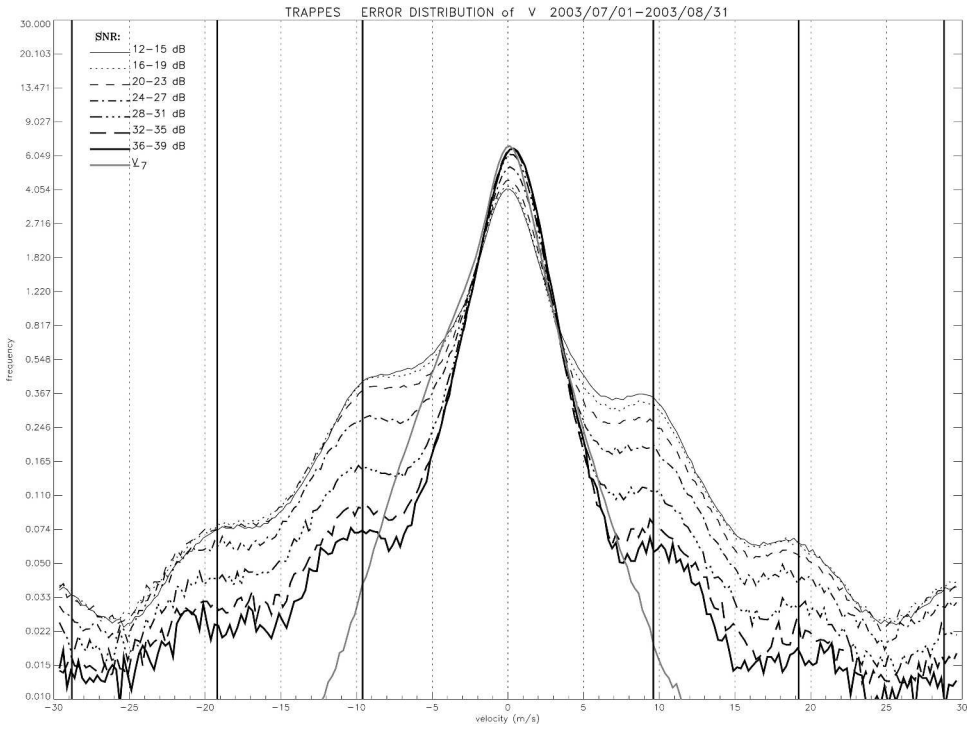

FIG. 9. Error structure of the combined velocity V_{combined} for different values of SNR. The error structure of the 7 km × 7 km median filtered velocity V_7 for all SNR values has been superimposed on the graph.

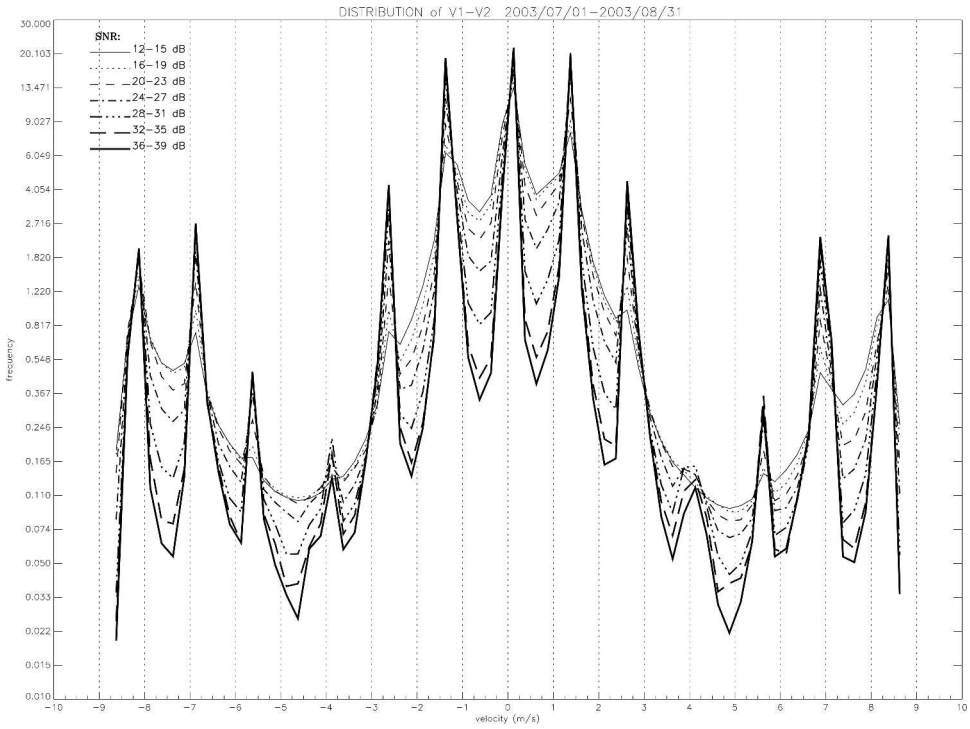

FIG. 10. Distribution of the velocity difference V_1–V_2 for different values of SNR.

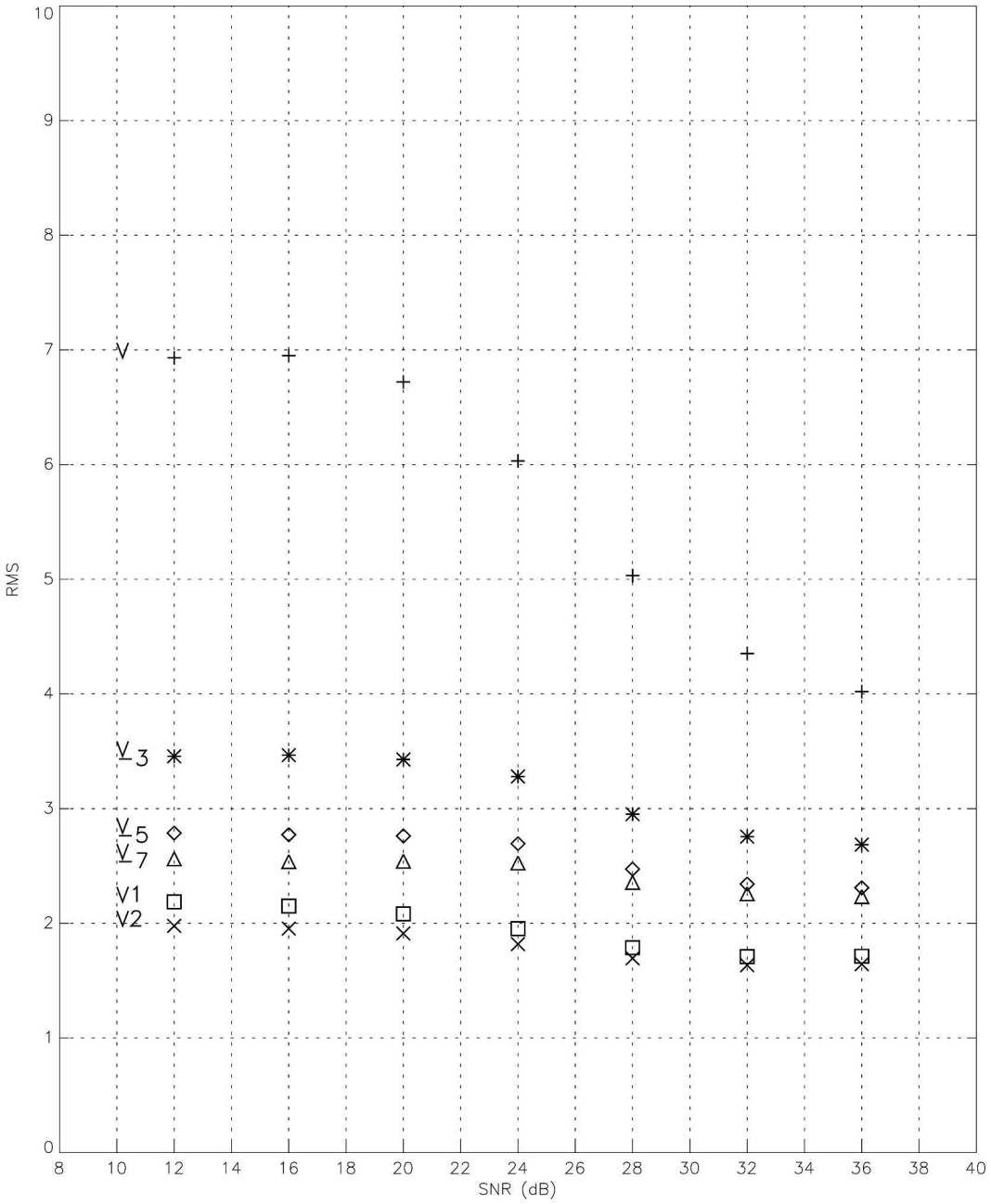

FIG. 11. Rms error of V_1, V_2, V, $\underline{V}_3$, $\underline{V}_5$, and $\underline{V}_7$ as a function of the SNR.

S-band radars with limited evolutionary potential, a constraint of the problem was to keep the two PRT close to the initial PRT of the radar (corresponding, for the Trappes C-band radar, to a PRF of 333 Hz). To extend the resulting Nyquist velocity up to 30 m s^{-1}, the two PRTs, PRT_1, and PRT_2, were set, respectively, to 1/360 and 1/310 s, in a ratio of 6/7—that is, very close to unity. The three Nyquist velocities, V_{N1}, V_{N2}, and V_N, are respectively equal to 4.8, 4.1, and 29.8 m s^{-1}. In the French context, the Doppler information will essentially be used up to 30 km to retrieve a VAD wind profile and up to 100 km for data assimilation purposes. In both cases, a spatial resolution of, say, 5 km $\times$ 5 km is quite sufficient.

Using quality-checked VAD profiles as the reference up to 30 km away from the radar, the statistical error distributions of the various velocities (velocity V_1 at lag PRT_1, velocity V_2 at lag PRT_2, and combined velocity V_{combined}) have been inferred as a function of the signal-to-noise ratio (SNR). Given the methodology and the fact that the VAD wind profiles might not be exactly representative of the actual wind field, all errors

should be considered as upper bounds. Consistently with theoretical results, the error distributions of V_1 and V_2, close to Gaussian, become more peaked as the SNR increases. The error distribution of V_{combined} evidences a large Gaussian maximum around 0 m s^{-1} but also a series of secondary maxima shifted exactly by $\pm 2k \times V_{N1}$ around 0, clearly identified as dealiasing errors. As the SNR increases, the main change in the V_{combined} error distribution is the attenuation of these side maxima. The histogram of V_1–V_2 has also been computed and reveals as theoretically expected a series of 13 peaks at 0, $\pm(-2V_{N2})$, $\pm(2V_{N1}-2V_{N2})$, $\pm(2V_{N1}-4V_{N2})$, $\pm(4V_{N1}-4V_{N2})$, $\pm(4V_{N1}-6V_{N2})$, and $\pm(6V_{N1}-6V_{N2})$. An increase in the SNR leads to a better separation between the peaks. A quality control might be introduced based on the difference between the actual velocity difference V_1–V_2 and the closest possible theoretical value. All in all, the scheme performs rather well despite the fact that the two PRT are in a ratio that is very close to unity. The key of the success is probably due to the slow antenna rotation rate on the one hand and to the interleaving of the radar pulses (i.e., dual PRT vs dual PRF) on the other hand. However, we did not attempt to quantify the relative weight of each factor and cannot therefore guarantee that the same scheme would work either with fast-scanning radars or with dual-PRF systems.

The implementation of a 7 km × 7 km median filter proves to be quite efficient to reduce dealiasing errors. The resulting rms error on the radial velocity, almost independent on the SNR, is about 2.2 m s^{-1}, again to be considered as an upper bound. As a second validation step, the quality of the retrieved wind profile will be assessed by comparison with collocated radiosondes and VHF wind profiler measurements. The profiles are also currently being monitored by the French operational ARPEGE weather forecast model, as a preliminary step before their assimilation. Pending the results, the scheme will be implemented, with minor modifications, on some C-band and S-band radars of the French radar network. The statistical availability of the wind profiles as a function of height has been computed over two periods July–August 2003 (summer) and September–November 2003 (fall). In the summer (fall), wind measurements are available 90% (75%) of the time at 500 m, 80% (55%) at 1000 m, 60% (35%) at 1500 m, 35% (25%) at 2000 m, and 6% (13%) above 4 km, which corresponds to the statistical occurrence of rain.

Acknowledgments. This work was done in the frame of the French PANTHERE (Project Programme Aramis Nouvelles Technologies en Hydrométéorologie Extension et REnouvellement) supported by Météo France, the French Ministère de l'Ecologie et du Développement Durable and the European Regional Development Fund (ERDF) of the European Union. We thank the two anonymous referees for their helpful comments and suggestions.

REFERENCES

Browning, K. A., and R. Wexler, 1968: The determination of kinematic properties of a wind field using Doppler radar. *J. Appl. Meteor.,* **7,** 105–113.

Curtis, J. N., and R. A. Houze, 2001: A real-time four-dimensional Doppler dealiasing scheme. *J. Atmos. Oceanic Technol.,* **18,** 1674–1683.

Doviak, R. J., and D. S. Zrnic, 1984: *Doppler Radar and Weather Observations.* Academic Press, 458 pp.

Gray, G., B. Lewis, J. Vinson, and F. Pratte, 1989: A real-time implementation of staggered PRT velocity unfolding. *J. Atmos. Oceanic Technol.,* **6,** 186–187.

Holleman, I., 2003: Quality of weather radar wind profiles. KNMI Scientific Rep. WR-2003-02, 72 pp.

——, and H. Beekhuis, 2003: Analysis and correction of dual-PRF velocity data. *J. Atmos. Oceanic Technol.,* **20,** 443–453.

Joe, P., and P. T. May, 2003: Correction of dual PRF velocity errors for operational Doppler weather radars. *J. Atmos. Oceanic Technol.,* **20,** 429–442.

Lindskog, M., H. Järvinen, and D. B. Michelson, 2000: Assimilation of radar radial winds in the HIRLAM 3D-VAR. *Phys. Chem. Earth,* **25,** 1243–1249.

Sachidananda, M., and D. S. Zrnic, 2002: An improved clutter filtering and spectral moment estimation algorithm for staggered PRT sequences. *J. Atmos. Oceanic Technol.,* **19,** 2009–2019.

Sugier, J., J. Parent-du-Châtelet, P. Roquain, and A. Smith, 2002: Detection and removal of clutter and anaprop in radar data using a statistical scheme based on echo fluctuation. *Proc. Second European Radar Conf., Copernicus GmbH,* Delft, Netherlands, 17–24.

Tabary, P., G. Scialom, and U. Germann, 2001: Real-time retrieval of the wind from aliased velocities measured by Doppler radars. *J. Atmos. Oceanic Technol.,* **18,** 875–882.

Waldteufel, P., and H. Corbin, 1979: On the analysis of single Doppler radar data. *J. Appl. Meteor.,* **18,** 534–542.

Zrnic, D. S., and P. Mahapatra, 1985: Two methods of ambiguity resolution in pulse Doppler weather radars. *IEEE Trans. Aerosp. Electron. Syst.,* **21,** 470–483.

——, and A. Zahrai, 2003: Evolution of weather surveillance radars, NSSL's perspective. *Proc. 31st Conf. on Radar Meteorology,* Seattle, WA, Amer. Meteor. Soc., 939–941.